Unsteady hydrodynamics of a full-scale tidal turbines

6th European Conference on Computational Mechanics (ECCM 6)
7th European Conference on Computational Fluid Dynamics (ECFD 7)
1115 June 2018, Glasgow, UK

UNSTEADY HYDRODYNAMICS OF A FULL-SCALE TIDAL TURBINE

Gabriel T Scarlett[1], Brian Sellar[1], Ton van den Bremer[2] Ignazio Maria Viola[1]

[1] School of Engineering, Institute for Energy Systems, The University of Edinburgh
Edinburgh, UK, EH9 3DW

[2] Department of Engineering Science, University of Oxford
Parks Road, Oxford, UK, OX1 3PJ

Key words: tidal turbine hydrodynamics, fatigue load, full-scale wave conditions, unsteady aerodynamics, blade element momentum theory, dynamic stall

Abstract. The rotation of a tidal turbine blade through an unsteady flow field can induce stall delay, load hysterisis and dynamic stall, where the shedding of a leading edge vortex may cause overshoots in lift more than twice that of the quasi-steady value. The significance of these effects for a full-scale tidal turbine rotor operating in realistic wave conditions has yet to be quantified. To investigate, we develop a model which couples dynamic stall, rotational augmentation and blade-element momentum theory with real flow measurements taken during large waves. For a 9 m diameter rotor operating at an optimal tip-speed ratio of 4.5, we find that the flow field is dominated by waves and that flow separation and dynamic stall are confined to sections near the hub. Unsteady attached flow phenomena caused a reduction in the lift available at the outboard sections near the tip which decreased the power coefficient by approximately 3% compared to the steady state value.

1 INTRODUCTION

Tidal current energy extraction is approaching a state of commercial readiness. Yet, questions remain regarding the performance and long term survivability of an axial flow tidal turbine rotor operating in the harsh marine environment [1].

The marine environment is inherently unsteady due to waves and turbulence. The rotation of the blade through the shear layer of the tidal current and the unsteady flow causes a time-dependent flow field which can lead to unsteady flow phenomena such as load hysteresis, stall delay and dynamic stall. Stall delay is when the angle of attack increases sufficiently rapidly that separation is prevented beyond the static stall angle and the lift increases beyond the maximum static value. Dynamic stall is when unsteady separation and stall occurs, resulting in a hysteresis loop of the lift with the angle of attack. These effects compounded with rotational forces and velocities induced by the dynamic wake behind the rotor make for a highly unsteady operational environment.

To date the quantification of unsteady loading on tidal turbine blades has been confined to scale models. Tully and Viola [2] carried out experiments on a scaled blade section in a wave flume tank and noted that the normal force experienced during waves can exceed the steady state value by more than 20%. Milne *et al.* [3, 4] carried out experiments on a scaled turbine by oscillating it in a towing tank. At lower tip-speed ratios, they found the flow was largely separated over the blade span, which for high-frequency forcing caused the root bending moment to exceed the quasi-steady value by up to 25% due to DS. Galloway *et al.* [5] tested the effects of a yaw misalignment and waves using a wave tank to generate linear waves. The experimental results showed that the median value of the root bending moment was exceeded by up to 175% during the presence of large waves. The authors concluded that the effect of DS was limited and, therefore can be neglected in some cases, despite not making comparison with quasi-steady values. These results are not in agreement with Milne *et al.*

Other than the work of Milne *et al.* [4], no documentation of DS occurring on tidal turbine blades exists. Yet, it is known to occur on all type of horizontal-axis wind turbines where skewed flow, shear, turbulence or tower shadow effects are present [6]. Since tidal turbine blades will also experience these effects with the addition of waves, it is likely that dynamic stall occurs. In addition, the difference between the mean value and the steady state has yet to be quantified.

The aim of this work is to answer the following research question: How significant are the unsteady effects of very large, realistic waves on the flow around and the loads on a tidal turbine blade? We investigate this by developing a model which couples state-of-the-art blade element momentum (BEM), DS and rotational augmentation theory with velocity field measurements using an Acoustic Doppler Current Profiler (ADCP) at the EMEC test site during the ReDAPT project [7]. We find that even at a hub depth of 27 m, waves induce unsteady load phenomena ranging from low amplitude hysteresis at the outer sections to highly non-linear overshoots near the blade root, the significance of which is discussed in detail.

2 TURBINE SPECIFICATION

Dimensions of the 3-bladed, Tidal Generation Ltd. DEEPGEN IV 1 MW tidal turbine deployed at the EMEC test site during the ReDAPT project are used. Schematic views of the port and front sides of the turbine are shown in Figure 1. A Cartesian coordinate system is placed at the still water level (SWL), directly above the nose of the turbine hub. The freestream current velocity is in the x direction, y is the port side direction and z is the vertical coordinate positive above the SWL. A cylindrical coordinate system with origin at the hub describes the radial (r) position along the blade, which extends to tip (R), and the azimuthal angle of the blade (ψ), which tracks the position of the blade as it rotates anti-clockwise. Also shown are the radius of the hub (R_h), the water depth (d) and the distance from the hub to the SWL (z_0). Chord (c) and geometrical twist (β_g) distributions along the blade span have been taken from Gretton [8]. Each blade section comprises of a NREL S814 profile with a relative thickness of 24%.

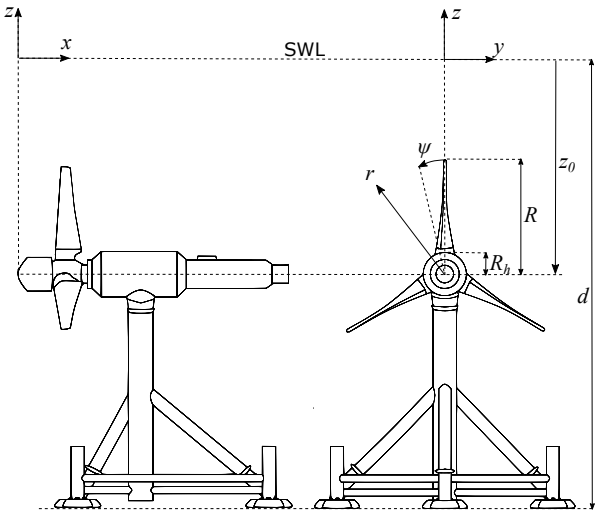

Figure 1: Schematic diagram of the tested tidal turbine (not to scale).

3 FORMULATION OF THE MODEL

3.1 Angle of attack time history

The velocity and force components acting on a blade section are computed as shown in Figure 2 (a) and (b), respectively. The relative velocity (W) is the magnitude of the difference between the axial velocity $U_x(1-a)$ and the tangential velocity $U_\psi(1+a')$, where a and a' are the axial and tangential induction factors, respectively, which account for velocities induced by the rotor wake. The angle of attack (α) is the angle that W makes with c, $\beta = \beta_g + \beta_p$ is the pitch angle which is measured between c and the rotor plane, where β_p is an operational pitch angle which may be applied to the blade. The flow angle is $\phi = \alpha + \beta$. The sectional drag force (F_D) which is codirectional with W and

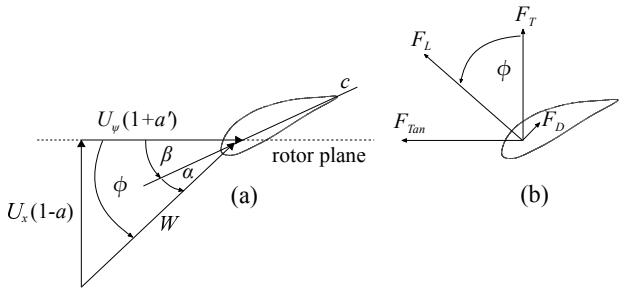

Figure 2: Blade section diagram showing (a) velocity components and (b) force components.

the lift force (F_L) perpendicular to it are defined per unit length as

$$F_D = \frac{1}{2} C_D \rho W^2 c, \quad F_L = \frac{1}{2} C_L \rho W^2 c, \tag{1a, b}$$

where C_D and C_L are the sectional coefficients of drag and lift, respectively and ρ is the fluid density. The axial force known as thrust (F_T) is perpendicular to the rotor plane

and is responsible for the blade bending out of the y-plane. The tangential force (F_{Tan}) drives the turbine and causes bending around the x-axis.

The measured ADCP velocity data is interpolated in time (t) and z to determine both U_x and the depthwise velocity component (U_z) incident to each blade section for a given t. The z-coordinate of a blade section is $z_0 + r\sin(\psi - \theta)$, where θ is the phase lag from the leading blade, and U_ψ is $U_z\cos(\psi - \theta)$.

The induction factors are calculated by iteratively solving the BEM equations [9]. The present model uses the solution method of Ning [10], which utilises a residual equation to converge on ϕ rather than solving for both a and a'. This enables the use of a root solving algorithm, which guarantees convergence. Using the geometrical definition for ϕ shown in Figure 2 (a) the following residual equation is formed

$$R(\phi) = \frac{\sin(\phi)}{(1-a)} - \frac{\cos(\phi)}{\lambda_r'(1+a')}, \tag{2}$$

where $\lambda_r' = \frac{U_\psi}{U_x}$ is the instantaneous, local tip-speed ratio. The value of ϕ which satisfies $R(\phi) \leq 10^{-6}$ is determined and used in the following iteration. The process is repeated until $R(\phi) \leq 10^{-6}$. With the induction factors solved for each time step, they are time averaged over the rotational period (T_r).

3.2 Dynamic load coefficients

The non-linear load coefficients are determined using the dynamic stall model of Sheng *et al.* [11]. This DS model is based on the 3rd generation dynamic stall model of Beddoes [12], but with a number of adaptations made to achieve better prediction at the lower Mach numbers associated with wind turbines. We modify the model to account for the effects of blade rotation and use definition for the unsteady drag coefficient given by Hansen *et al.* [13].

The total unsteady load response comprises of three elements: attached flow, trailing edge separation and leading edge vortex shedding, which we will now discuss.

Load response in attached flow

The linear lift coefficient comprises of both circulatory and non-circulatory components. The latter accounts for flow acceleration effects and the former for circulation around the foil and vorticity shed into the wake, which introduces a phase lag and amplitude reduction from the quasi-steady value. The attached loads are determined using the incompressible time domain solution of Wagner [14], which gives the circulatory lift coefficient ($C_L^c = 2\pi\alpha_E$), where α_E is the equivalent angle of attack determined by superposition of step changes in α through the Duhamel integral as follows

$$\alpha_E = \alpha(0)\Phi(s) + \int_0^s \frac{\mathrm{d}\alpha(\sigma)}{\mathrm{d}t}\Phi(s-\sigma)\mathrm{d}\sigma, \tag{3}$$

where $\Phi(s)$ is the Wagner function, its argument $s = \frac{2U_0 t}{c}$ is the non-dimensional time and σ is a dummy time variable of integration. Wagner does not give a convenient analytical

solution to $\Phi(s)$. Therefore, the following exponential approximation given by Jones [15] is used

$$\Phi(s) \approx 1 - 0.1652e^{-0.0455s} - 0.335e^{-0.3s}. \tag{4}$$

The non-circulatory coefficient (C_L^{nc}), i.e. the added mass, is treated outside of the Duhamel integral. For this term we use the approximation given by Hansen *et al.* [13], where

$$C_L^{nc} = \frac{\pi c \dot{\alpha}}{2U_0}. \tag{5}$$

Then the full lift coefficient in attached flow $C_L^p = C_L^c + C_L^{nc}$. For an arbitrary α forcing Equation 3 and Equation 5 are determined numerically.

Load response in separated flow

The first part of the non-linear solution is the load response in separated flow. To quantify this, Kirchhoff theory ([16, p. 170]) is used, which relates the position of the trailing-edge separation point (f) to the static normal force coefficient C_N. f is normalised by the chord length (c), as illustrated in Figure 3, where x is the dimensional coordinate. When the boundary layer is fully attached, $f = 1$, and when fully separated, $f = 0$.

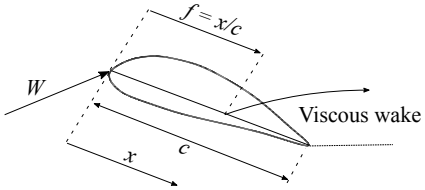

Figure 3: Trailing-edge separation point described by Kirchhoff flow past a flat plate.

The relationship between C_N, α and f is

$$C_N = C_{N_\alpha}(\alpha - \alpha_0)\Big(\frac{1+\sqrt{f}}{2}\Big)^2, \tag{6}$$

where $C_{N_\alpha} = \frac{\mathrm{d}C_N}{\mathrm{d}\alpha}|_{\alpha_0}$ is the slope evaluated at the angle of zero lift (α_0). Equation 6 is rearranged to solve for f using static wind tunnel test data for C_N [17]. Then, f is determined for any α using a look-up table. Under unsteady conditions, boundary layer separation is delayed to a higher value of α. We can model this angle (α') as a first-order lag in the s domain, namely

$$\frac{\mathrm{d}\alpha'}{\mathrm{d}s} = -\frac{(\alpha' - \alpha)}{T_\alpha}, \tag{7}$$

where T_α is an empirical time constant describing the angle of attack delay. With α' determined, the dynamic separation point f' is found using the look-up table and replacing α as follows

$$f'(\alpha) = f(\alpha' - \Delta\alpha_1), \tag{8}$$

where $\Delta\alpha_1$ is a shift delay from the static stall angle (α_{ss}) defined $\Delta\alpha_1 = \alpha_{cr} - \alpha_{ss}$, α_{cr} is the critical angle of dynamic stall onset.

Dynamic stall load response

Dynamic stall onset occurs once $\alpha' \geq \alpha_{cr}$, after which an additional lag in the separation point occurs, as the leading edge vortex forms causing an additional load overshoot. This is implemented by applying a first-order lag to the dynamic separation point as

$$\frac{\mathrm{d}f''}{\mathrm{d}s} = -\frac{(f'' - f')}{T_v}, \tag{9}$$

where T_v is the vortex time constant which includes both the formation and convection time. Vortex shedding follows the method of Beddoes [12], which uses a vortex shape function (V_x) defined

$$V_x = \begin{cases} \sin^{3/2}\left(\frac{\pi\tau}{2T_v}\right), & 0 < \tau \leq T_v \\ \\ \cos^2\left(\frac{\pi(\tau - T_v)}{T_{vL}}\right), & T_v < \tau, \end{cases} \tag{10}$$

where τ is the non-dimensional vortex passage time which increases from zero at the onset of dynamic stall, and T_{vL} is the speed of the vortex convection. The additional lift contribution is then given as the difference between the delayed and the static separation points multiplied by the shape function as follows

$$C_N^v = B(f' - f)V_x, \tag{11}$$

where B is a constant dependent on aerofoil geometry.

Non-linear force coefficients

The final expression for the normal force coefficient C_N is

$$C_N^u = C_N^c\left(\frac{1 + \sqrt{f''}}{2}\right)^2 + C_N^{nc} + C_N^v. \tag{12}$$

The expression for the chordwise force coefficient is

$$C_C^u = \eta C_{N\alpha}(\alpha_E - \alpha_0)^2(\sqrt{f'} - E_0), \tag{13}$$

which has no contribution from the vortex. The parameters η and E_0 are both dependent on the sectional geometry. The lift coefficient is then

$$C_L^u = C_N^u \cos(\alpha) + C_C^u \sin(\alpha). \tag{14}$$

The unsteady drag coefficient C_D^u is determined using the model of Hansen *et al.* [18], which is expressed as three terms

$$C_D^u = C_D^{st} + C_D^{ind} + C_D^{vis}, \tag{15}$$

where

$$C_D^{ind} = C_L^u(\alpha - \alpha_E), \tag{16}$$

and

$$C_D^{vis} = (C_D^{st} - C_{D0})\Big(\frac{1+\sqrt{f''}}{2}\Big)^2 - \Big(\frac{1+\sqrt{f(\alpha_E)}}{2}\Big)^2, \tag{17}$$

where C_D^{st} is the static drag coefficient and C_{D0} the drag coefficient at α_0. The three terms on the right hand side of Equation 15 are the static, induced and viscous components of drag respectively.

The empirical parameters for the NREL S814 are given in Table 1. They are taken from [19], with slight modifications made using the Ohio State University (OSU) wind tunnel test data [17].

Table 1: Table of empirical parameters for the NREL S814

α_{cr}	0.2426
α_{ss}	0.2007
α_0	-0.0573
C_{D0}	0.01
$C_{N\alpha}$	6.267
E_0	0.1
η	1
T_α	6.33
T_v	4
T_{vL}	6
B	0.5

3.3 Rotational augmentation

Rotation of the blades induces a centrifugal force which causes a spanwise flow and a Coriolis force which accelerates the flow towards the trailing edge. These effects reduce the adverse pressure gradient to promote flow reattachment and delay separation, which in turn leads to lift augmentation from the stationary value [20]. The phenomena is not very well understood and modelling techniques have had mixed success. To date only one full scale experiment has been carried out. The NREL Phase VI test investigated the effects of both unsteadiness and rotation on a 10 m diameter wind turbine employing NREL S809 profiles [21]. The study found that for inboard blade sections both lift and drag force are augmented compared to a non-rotating blade. However, conversely, for outer blade sections, both lift and drag are reduced. Modeling this behavior is a challenge. Breton *et al.* [22] tested the prediction capabilities of a number of rotational augmentation models to predict the NREL Phase VI test data. Their study determined that none of the models could satisfactorily predict C_L and C_D across the entire blade span, and that only the Lindenburg model [23] successfully captured a reduction in C_L at the outer sections. The Lindenburg model is well-suited to combination with the DS model since both use the separation point parameter f. To this end, we implement Lindenburg's model by correcting the 2D aerofoil parameters used to determine the unsteady force coefficients.

4 VALIDATION OF THE MODEL

We validated the key components of the numerical model as follows. First, the BEM implementation is used to predict values of power (C_P) and thrust (C_T) coefficients respectively for varying tip-speed ratios (λ) $\in \{0.5, 8\}$, which are compared to those predictied using AeroDyn, an opensource aerodynamic software developed by NREL, which also uses the theoretical implementation of Ning *et al.* [24]. The turbine employs uniform thickness NREL S814 profiles at each section, the flow is steady with a current velocity of 2.77 ms^{-1}, the rotor is normal to the flow and $\beta_p = 0$. The results are shown in Figure 4 (a) and (b) for C_P and C_T respectively. The predicted values of C_P are in very good agreement with that of AeroDyn up until $\lambda = 5$, after which the value is slightly under predicted compared to AeroDyn, although both have similarly decreasing slopes. The predicted values of C_T agree well across the full range, apart from a slight over prediction for $\lambda \in \{4, 5\}$. These results verify that the BEM implementation is performing as expected.

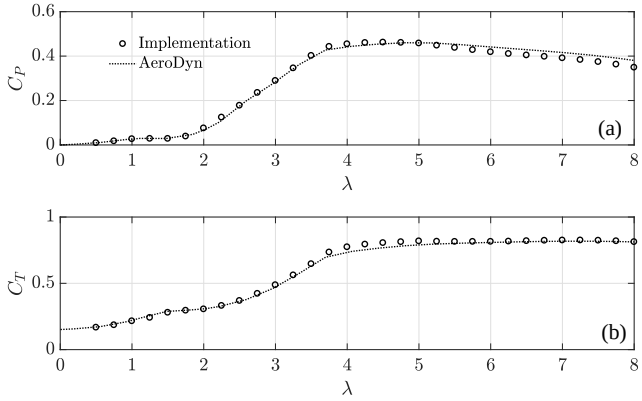

Figure 4: Power (a) and thrust (b) coefficient performance curves for a turbine operating in steady conditions.

Next, the predictive capabilities of the DS model are tested. The relationship between C_L and α for the S814 aerofoil is shown in Figure 5 for a number of cases. Empirical values from the OSU wind tunnel tests are shown for the static and dynamic non-rotational cases (2D) [17]. Predicted values are shown for the dynamic (2D) case, and for both the static and dynamic rotational (3D) cases. The forcing is a pitching motion of $13.8° + 10.75° \sin(\omega t)$, the reduced frequency, defined $k_r = \frac{2\pi\omega c}{W}$ is 0.091, and for the rotational case, $r = 0.47R$. The 2D dynamic model predicts the value of C_L when pitching positively from around 3° to 18° very well compared to the OSU dynamic data, and the shape of the load hysteresis matches qualitatively.

The model predicts an increase in lift at around 18° caused by vortex shedding, which leads to a peak of approximately 2.1. However, the model lags the measured value by about 1° leading to an overprediction. After the peak, stall occurs followed by a dramatic reduction in lift. The predicted data follows the trend of the measured value by briefly recovering from stall at around 23°, which is likely due to a secondary vortex shedding.

The measured data follows a similar trend, with a slight recovery occurring at around 22°. During the return from stall, when α is decreasing the model overpredicts C_L. The

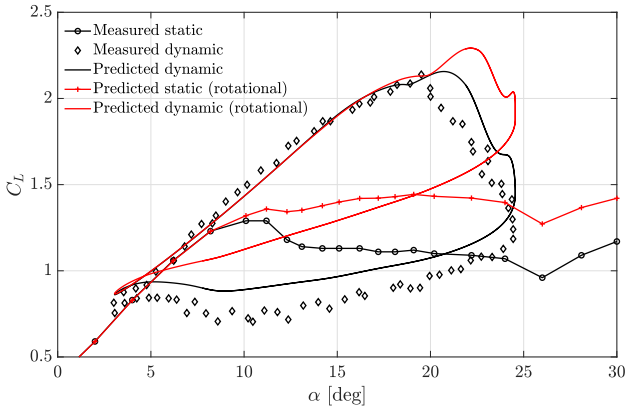

Figure 5: Lift coefficient against angle of attack for steady, dynamic and rotational conditions.

modification made to combine the effects of DS with rotational augmentation cannot easily be validated since no dynamic 3D data exists for the NREL S814. However, a qualitative comparison can be made using the NREL Phase VI experimental data for the S809. The difference in the experimental results between the rotating and non-rotating cases shown in [25] agrees qualitatively with the difference between the dynamic 2D and 3D curves in Figure 5.

5 CASE STUDY

In this study a 256 s flow sample measured at EMEC on the 22nd of November 2014 is used. The sample was selected on the basis of it containing an energetic wave train and to investigate the unsteady hydrodynamic response of the rotor. The free surface elevation (η) is measured at a fixed point in space directly above the turbine nacelle. The η time history is shown over 250 s in Figure 6 (a). The sample is characterised by having maximum wave height of approximately 5 m and apparent wave period of 10 s. The wave steepness, defined as the product of wave amplitude and wave number is approximately 0.17, indicating that the wave is weakly non-linear. The power spectral density (S) of η, shown in Figure 6 (b), confirms that the energy contained within this wave group is centred around 0.095 Hz. Streamwise (U_x) and depthwise (U_z) velocities are measured from the bed to the SWL in 1 m increments at a sampling frequency of 0.5 Hz, where $d = 45$ m, and $z_0 = -27$ m. The location of the ADCP is approximately $y = -40$ m. Measurement techniques and data processing are discussed in more depth in [26].

The time-averaged U_x depth profile from 3 m above the bed ($z = -42$ m) to the SWL is shown in Figure 7 (a). The current velocity depth profile of U_x follows a power law with exponent 0.153, and hub velocity of 2.71 ms^{-1}. The power spectral density of U_x is shown in Figure 7 (b). Noticeably, the peak frequency in the velocity spectrum at both $z = -18$ m and $z = -27$ m correspond to the 0.095 Hz value found in the η spectrum.

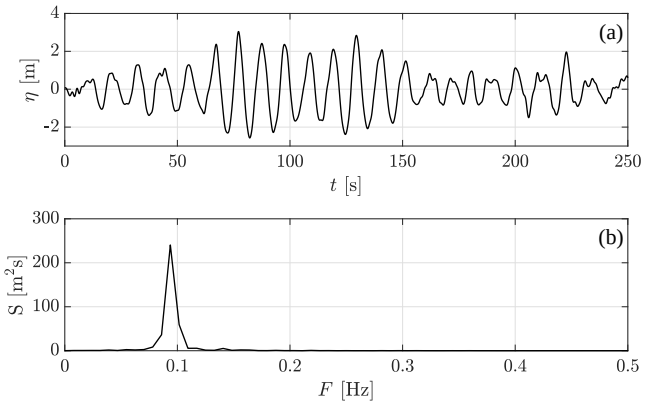

Figure 6: Freesurface elevation (a) time history and (b) power spectral density

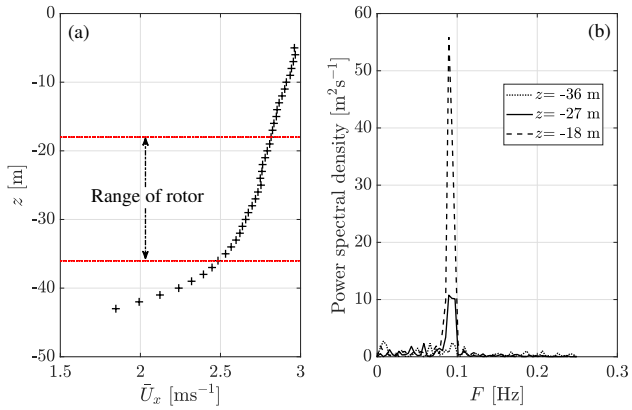

Figure 7: Plot of (a) the time-averaged depth profile of the streamwise velocity and (b) the power spectral density of the streamwise velocity encountered at the minimum ($z = -18$ m), hub ($z = -27$ m) and maximum ($z = -36$ m) depth ranges of the turbine blade.

6 RESULTS

6.1 Rotor performance

The magnitude of U_x averaged over the swept area and the sample time period is $\bar{U_x} = 2.72$ ms^{-1}, while $\sqrt{\bar{U_x^2}} = 2.74$ ms^{-1} and $\sqrt[3]{\bar{U_x^3}} = 2.77$ ms^{-1}. The latter velocity is used for the steady simulation and to nondimensionalise forces, torque and power. The operating parameters λ and β_p, which yield a maximum C_P in a steady current $U_0 = 2.77$ ms^{-1} are determined using the BEM model with static coefficients corrected for rotation. A peak $C_P = 0.47$ occurs when $\lambda = 4.5$ and $\beta_p = 0.1°$, with $C_T = 0.81$. All subsequent simulations are carried out with these parameters.

Values of C_P and C_T simulated over the full time period of 256 s for both steady and unsteady conditions, as shown in Figure 8 for 10 rotational periods ($T_r = 4.5$ s). Where the steady value has been computed using static wind tunnel data [17]. Comparing the mean value of the unsteady time history with the steady value shows a power decrease of 3% and a thrust decrease of 3% from the steady-state. Unsteadiness is clearly dominated

by the period of the wave, with no discernible contribution from T_r.

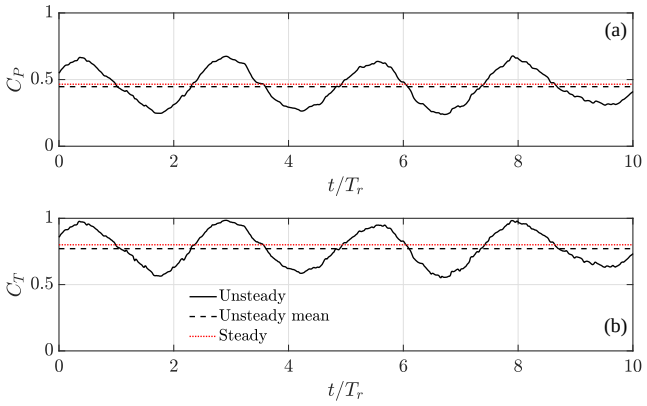

Figure 8: Comparison of (a) power coefficient and (b) thrust coefficient over 10 blade rotations, showing the predicted unsteady time history, and corresponding mean value alongside steady-state response.

Time averaged, sectional values for the lift ($\bar{C_L}$), drag ($\bar{C_D}$), thrust ($\bar{C_T}$) and torque ($\bar{C_Q}$) coefficients are shown in Figure 9 a, b, c and d, respectively for the steady, quasi-steady and unsteady predictions. The quasi-steady values are determined using static wind tunnel data [17]. We note that both the steady and quasi-steady values of $\bar{C_L}$ are greater at the outer sections and lower at the inner sections compared to the unsteady prediction, which indicates that linear unsteady phenomena are reducing $\bar{C_L}$ at the inner sections and non-linear unsteady effects are increasing it inboard of the mid-section. An increase in the unsteady value of $\bar{C_D}$ occurs near the blade root where the flow is highly separated, however, from about $0.3R$ it follows the steady value. The unsteady value of $\bar{C_T}$ is reduced at the outer blade sections, which compounded with the higher dynamic pressure and longer moment arm at the tip, reduces the rotor thrust load. Likewise unsteady $\bar{C_Q}$ is less from about $0.3R$ to R than under steady conditions which explains the reduction in C_P.

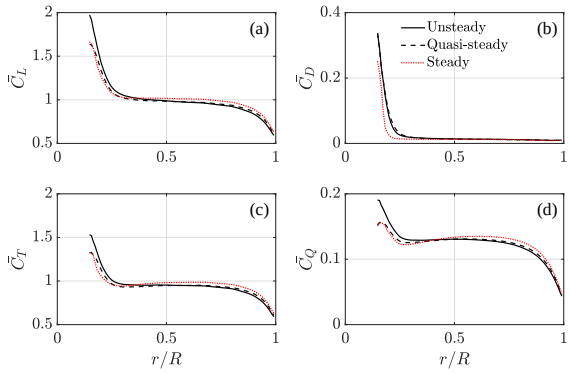

Figure 9: Comparison of mean (a) lift coefficient, (b) drag coefficient, (c) thrust coefficient and (d) torque coefficient along the blade span for steady, quasi-steady and unsteady conditions.

6.2 Unsteady flow along the blade span

Time histories for f, α and C_L are shown in Figure 10 at locations $0.15R$, $0.4R$ and $0.96R$ on the blade. Near the tip ($0.96R$), the separation point is a constant and equal to unity, indicating that no separation occurs, which is confirmed by the moderate α fluctuations which remain inside the attached flow region (-8° to 8°). The associated unsteady C_L is slightly below the quasi-steady value due to the shedding of vorticity from the trailing edge, which causes a phase lag and amplitude reduction. At the mid-section ($0.4R$) the flow remains attached under steady and unsteady conditions. However, moderate separation is evident for the quasi-steady case. The unsteady value of α is in excess of 8°. However, unsteady phenomena reduces the adverse pressure gradient in the boundary layer, causing a delay in separation from the quasi-steady value [27], which explains why the amplitude of unsteady C_L now exceeds the quasi-steady value. The separation point near the blade root ($0.15R$) is a constant 0.7 under steady conditions. The unsteady mean value and amplitude for f is less than the quasi-steady value indicating that highly non-linear phenomena are occurring. The α history shows that the oscillations are almost completely outside of the linear region. The instantaneous C_L computed with the unsteady approach was up to 98% and 71% greater than C_L computed with a quasi-steady and a steady approach, respectively. The large unsteady C_L value is due to the formation and shedding of the leading-edge vortex

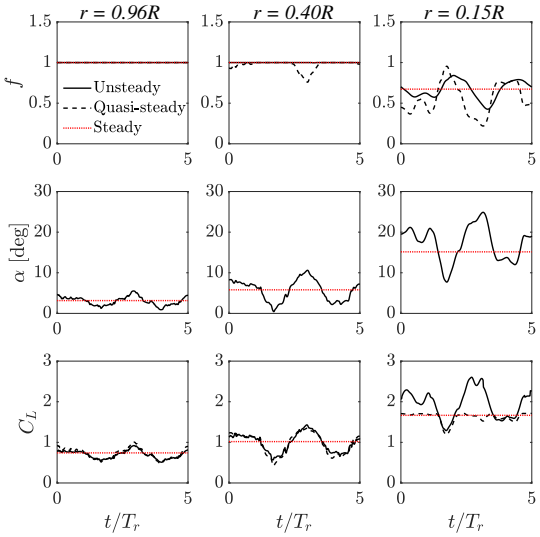

Figure 10: Time histories for separation point, angle of attack and lift coefficient at blade locations near the tip ($r = 0.96R$), mid-section ($r = 0.40R$) and root ($r = 0.15R$).

7 CONCLUSIONS

A model has been developed and solved numerically quantifying the performance of a full-scale tidal turbine operating during large wave events. The angle of attack on the blade is determined using velocity measurements made at the EMEC test site, along with

a blade-element momentum model to determine the velocities induced by the wake. The unsteady load coefficients are determined using a dynamic stall model, which we modified to include rotational flow augmentation.

The unsteady flow is dominated by large waves of 0.17 steepness centred around a frequency of 0.095 Hz, which dictate the unsteady hydrodynamics on the tidal turbine rotor.

Unsteady flow phenomena manifest themselves as an attached-flow phase lag and amplitude reduction at the outer blade sections towards the tip. Towards the mid-section, a delay in flow separation occurs, causing a small increase above the quasi-steady value. Near the blade root dynamic stall causes the unsteady lift coefficient to exceed the steady value by approximately 70% and the quasi-steady value by almost 100%.

In unsteady conditions, the mean power and thrust coefficients are both reduced by approximately 3% from the steady state. This is caused by the reduction in lift near the tip due to unsteady effects in attached flow conditions.

ACKNOWLEDGEMENT

The first named author is supported by an Engineering and Physical Sciences Research Council grant. Field measurements were acquired under the ReDAPT project (2010-2015) which was co-funded by the Energy Technologies Institute (ETI), UK.

REFERENCES

[1] L. Chen and W.-H. Lam, "A review of survivability and remedial actions of tidal current turbines," *Renewable and Sustainable Energy Reviews*, vol. 43, pp. 891–900, 2015.

[2] S. Tully and I. M. Viola, "Reducing the wave induced loading of tidal turbine blades through the use of a flexible blade," *International Symposium on Transport Phenomena and Dynamics of Rotating Machinery (ISROMAC 2016)*, p. 9, 2016.

[3] I. A. Milne, A. H. Day, R. N. Sharma, and R. G. J. Flay, "Blade loads on tidal turbines in planar oscillatory flow," *Ocean Engineering*, vol. 60, pp. 163–174, 2013.

[4] I. A. Milne, A. H. Day, R. N. Sharma, and R. G. J. Flay, "The characterisation of the hydrodynamic loads on tidal turbines due to turbulence," *Renewable and Sustainable Energy Reviews*, vol. 56, pp. 851–864, 2016.

[5] P. W. Galloway, L. E. Myers, and A. S. Bahaj, "Quantifying wave and yaw effects on a scale tidal stream turbine," *Renewable Energy*, vol. 63, pp. 297–307, 2014.

[6] C. P. Butterfield, A. C. Hansen, D. Simms, and G. Scott, "Dynamic stall on wind turbine blades," tech. rep., National Renewable Energy Lab., Golden, CO (United States), 1991.

[7] B. Sellar, "Metocean Data Set from the ReDAPT Tidal Project: Batch 1, Part 2, 2011-2014," tech. rep., University of Edinburgh, 2016.

[8] G. I. Gretton, "Development of a computational fluid dynamics model for a horizontal axis tidal current turbine," Tech. Rep. WG3 WP5 D1, 2010.

[9] T. Burton, N. Jenkins, D. Sharpe, and E. Bossanyi, *Wind Energy Handbook*. Chichester, UK: John Wiley & Sons, Ltd, may 2011.

[10] A. S. Ning, "A simple solution method for the blade element momentum equations with guaranteed convergence," *Wind Energy*, vol. 17, pp. 1327–1345, jul 2014.

[11] W. Sheng, R. A. M. Galbraith, and F. N. Coton, "A modified dynamic stall model for low Mach numbers," *Journal of Solar Energy Engineering*, vol. 130, no. 3, p. 031013, 2008.

[12] T. S. Beddoes, "A third generation model for unsteady aerodynamics and dynamic stall," tech. rep., Westland Helicopters Limited, 1993.

[13] M. H. Hansen, M. Gaunaa, and H. A. Madsen, "A Beddoes-Leishman type dynamic stall model in state-space and indicial formulations," tech. rep., 2004.

[14] H. Wagner, "Über die entstehung des dynamischen auftriebes von tragflügeln," *Journal of Applied Mathematics and Mechanics/Zeitschrift für Angewandte Mathematik und Mechanik*, vol. 5, no. 1, pp. 17–35, 1925.

[15] R. T. Jones, "The unsteady lift of a wing of finite aspect ratio," *NACA Report 681*, 1940.

[16] B. Thwaites, *Incompressible Aerodynamics: An account of the theory and observations of the steady flow of incompressible fluid past aerofoils, wings and other bodies*. University Oxford Press, 1960.

[17] J. M. Janiszewska, R. Reuss Ramsay, M. J. Hoffmann, and G. M. Gregorek, "Effects of grit roughness and pitch oscillations on the S814 airfoil," tech. rep., 1996.

[18] M. Hansen, J. Sørensen, S. Voutsinas, N. Sørensen, and H. Madsen, "State of the art in wind turbine aerodynamics and aeroelasticity," *Progress in Aerospace Sciences*, vol. 42, pp. 285–330, jun 2006.

[19] W. Sheng, R. A. M. Galbraith, and F. N. Coton, "Applications of low-speed dynamic-stall model to the NREL airfoils," *Journal of Solar Energy Engineering*, vol. 132, no. 1, p. 011006, 2010.

[20] Z. Du and M. Selig, "The effect of rotation on the boundary layer of a wind turbine blade," *Renewable Energy*, vol. 20, pp. 167–181, jun 2000.

[21] M. M. Hand, D. a. Simms, L. J. Fingersh, D. W. Jager, J. R. Cotrell, S. Schreck, and S. M. Larwood, "Unsteady aerodynamics experiment phase VI: wind tunnel test configurations and available data campaigns," Tech. Rep. December, National Renewable Energy Laboratory (NREL), Golden, CO, dec 2001.

[22] S.-P. Breton, F. N. Coton, and G. Moe, "A study on rotational effects and different stall delay models using a prescribed wake vortex scheme and NREL phase VI experiment data," *Wind Energy*, vol. 11, pp. 459–482, sep 2008.

[23] C. Lindenburg, "Modelling of rotational augmentation based on engineering considerations and measurements," in *European Wind Energy Conference*, pp. 22–25, 2004.

[24] A. Ning, G. Hayman, R. Damiani, and J. M. Jonkman, "Development and validation of a new blade element momentum skewed-wake model within AeroDyn," in *33rd Wind Energy Symposium*, no. December 2014, (Reston, Virginia), American Institute of Aeronautics and Astronautics, jan 2015.

[25] S. Guntur, N. N. Sørensen, S. Schreck, and L. Bergami, "Modeling dynamic stall on wind turbine blades under rotationally augmented flow fields," *Wind Energy*, vol. 19, pp. 383–397, mar 2016.

[26] D. S. D. I. Brian Sellar Gareth Wakelam and V. Venugopal, "Characterisation of tidal flows at the European Marine Energy Centre in the absence of ocean waves," *Energies*, vol. 11, no. (in review), 2017.

[27] L. Ericsson and J. Reding, "Fluid mechanics of dynamic stall part I. Unsteady flow concepts," *Journal of Fluids and Structures*, vol. 2, no. 1, pp. 1–33, 1988.